

# Journal of Materials Chemistry A

Materials for energy and sustainability

Accepted Manuscript

This article can be cited before page numbers have been issued, to do this please use: A. Donnadio, I. D'Ambrosio, G. Menendez Rodriguez, F. Costantino, R. Vivani, S. Giovagnoli, A. Macchioni, M. Nocchetti, E. Rodriguez-Castellon and B. Muzzi, *J. Mater. Chem. A*, 2026, DOI: 10.1039/D6TA01464J.



This is an Accepted Manuscript, which has been through the Royal Society of Chemistry peer review process and has been accepted for publication.

Accepted Manuscripts are published online shortly after acceptance, before technical editing, formatting and proof reading. Using this free service, authors can make their results available to the community, in citable form, before we publish the edited article. We will replace this Accepted Manuscript with the edited and formatted Advance Article as soon as it is available.

You can find more information about Accepted Manuscripts in the [Information for Authors](#).

Please note that technical editing may introduce minor changes to the text and/or graphics, which may alter content. The journal's standard [Terms & Conditions](#) and the [Ethical guidelines](#) still apply. In no event shall the Royal Society of Chemistry be held responsible for any errors or omissions in this Accepted Manuscript or any consequences arising from the use of any information it contains.

# Hybrid Zirconium Phosphate Phosphonates as Efficient Hosts for Confined Ni-Fe Oxygen Evolution Catalysts

View Article Online

DOI: 10.1039/D6TA01464J

Anna Donnadio,<sup>\*a</sup> Iolanda D'Ambrosio,<sup>b</sup> Gabriel Menendez Rodriguez,<sup>b,c</sup> Ferdinando Costantino,<sup>b</sup> Riccardo Vivani,<sup>a</sup> Stefano Giovagnoli,<sup>a</sup> Alceo Macchioni,<sup>b,c</sup> Beatrice Muzzi,<sup>d</sup> Enrique Rodríguez-Castellón<sup>e</sup>, Morena Nocchetti<sup>\*a</sup>

<sup>a</sup> Department of Pharmaceutical Sciences, University of Perugia, via del Liceo 1, 06123 Perugia, Italy

<sup>b</sup> Department of Chemistry, Biology and Biotechnologies, University of Perugia, via del Liceo 1, 06123 Perugia, Italy

<sup>c</sup> CIRCC, Interuniversity Consortium for Chemical Reactivity and Catalysis, Via C. Ulpiani, 27 - 70 126 Bari, Italy

<sup>d</sup> Institute of Chemistry of Organometallic Compounds - CNR, via Madonna del Piano, 10 50019 Sesto Fiorentino (FI), Italy

<sup>e</sup> Department of Inorganic Chemistry, Institute for Interuniversity Research in Bio-Refineries (I3B), Faculty of Sciences, University of Málaga, 29071 Málaga, Spain.

## Abstract

The rational design of earth-abundant electrocatalysts for the oxygen evolution reaction (OER) requires materials platforms capable of stabilizing catalytically active species under strongly alkaline conditions while maintaining efficient charge-transfer pathways. Here, we report a family of amino acid-derived zirconium phosphate–phosphonate hybrid materials that act as structurally tunable layered hosts for the confinement of Ni<sup>2+</sup> and Fe<sup>3+</sup> ions. Amino acid



functionalization promotes partial exfoliation of the layered framework into colloidal nanosheets, enabling homogeneous metal dispersion within well-defined organic–inorganic interfaces. Systematic variation of ligand structure and Ni/Fe composition reveals clear correlations between supramolecular organization, interfacial metal coordination, and electrocatalytic performance. The glycine-derived material (ZGLY) with an optimized Ni/Fe ratio achieves an overpotential of 304 mV to reach a geometric current density of 10 mA cm<sup>-2</sup> and a Tafel slope of 32.9 mV dec<sup>-1</sup>, together with sustained stability in alkaline media, exhibiting enhanced activity and overall performance compared to previously reported zirconium phosphate-based OER systems. Post-operando Raman spectroscopy and XPS unambiguously identify the NiOOH and FeOOH formed in situ as the catalytically active phases, while XRD and electron microscopy confirm that the ZPAC scaffold preserves its structural integrity throughout the operation. These observations indicate that the ZPAC framework primarily acts as a chemically robust host, enabling the stabilization and spatial confinement of the catalytically active Ni-Fe oxyhydroxide species formed under operating conditions. Consequently, these findings highlight zirconium phosphate–phosphonates as versatile 2D hybrid materials in which the chemical composition, interlayer organization, and metal confinement can be tuned to regulate catalytic behavior, providing new insights into the design of durable, earth-abundant water oxidation catalysts.

## 1. Introduction

Increasing global energy demand, the depletion of fossil fuels, and their negative environmental impact are driving research into clean and sustainable energy technologies. As an alternative to fossil fuels, hydrogen (H<sub>2</sub>) is considered a promising energy vector,<sup>1</sup> particularly when produced via direct electrochemical water splitting, which offers a sustainable and cost-effective pathway.<sup>2</sup> However, reducing the energy consumption of water



electrolysis remains a key challenge for the large-scale deployment of “green” hydrogen. Water electrolysis involves two half reactions: the cathodic hydrogen evolution reaction (HER) and the anodic oxygen evolution reaction (OER). HER is a relatively simple two-electron transport process involving electrochemical H<sup>+</sup> adsorption and desorption of H<sub>2</sub>. Conversely, OER is a more complex process with sluggish oxygen evolution kinetics that makes it the limiting half-reaction. In OER, four electrons and four protons have to be transferred in a multi-step reaction, each of which produces the formation of an intermediate. The formation of these intermediates introduces significant energy barriers, making OER the rate-limiting step and the primary contributor to the overpotential in water electrolysis.<sup>3,4</sup> Because of this, the rational design of catalysts capable of promoting OER by reducing its overpotential is a key task on the way to a widely applicable power-to-fuel scheme via water electrolysis. Until now, heterogeneous catalysts based on transition metals have been widely investigated because of their outstanding OER catalytic activity. Noble-metal oxides such as RuO<sub>2</sub> and IrO<sub>2</sub> remain benchmark OER catalysts.<sup>5,6</sup> However, their high cost, limited availability, and poor stability in strongly alkaline media restrict large-scale application. These limitations have driven significant interest in low-cost, earth-abundant alternatives, particularly first-row transition metals.<sup>7</sup> OER electrocatalysts based on Fe, Co, and Ni, in the form of oxides and (oxy)hydroxides, layered double hydroxides,<sup>8,9</sup> MXenes,<sup>10</sup> phosphates, dichalcogenides, nitrides, borides and carbides, have shown very high performance.<sup>5</sup> Interestingly, it has been observed that during OER, these catalysts transform into other oxide phases, generally metal (oxy)hydroxides (TMHOs), which perform better than the parent material.<sup>11</sup> The formation of these active phases in a confined environment, such as two-dimensional (2D) materials, is a recently proposed strategy to stabilise them, avoiding aggregation and making the active sites available. Among 2D materials, transition metal dichalcogenides,<sup>12,13</sup> layered (oxy)hydroxides,<sup>14</sup> graphene<sup>15</sup> and zirconium phosphate (ZrP)

View Article Online  
DOI: 10.1039/D6TA01464J



have been investigated.<sup>16</sup> The ion-exchange capability and electrochemical stability of ZrP make it an effective support for transition metal-based OER catalysts in alkaline media.<sup>17</sup>  $\alpha$ -ZrP with intercalated or adsorbed  $\text{Fe}^{2+}$ ,  $\text{Fe}^{3+}$ ,  $\text{Co}^{2+}$ , and  $\text{Ni}^{2+}$  ions showed interesting catalytic activity for the OER, requiring overpotentials of 0.5-0.7 V to achieve a current density of 10  $\text{mA cm}^{-2}$ . The catalytic performance of layered ZrP materials improves upon exfoliation, as OER predominantly occurs on the outer surfaces of the nanoparticles.<sup>18</sup> Moreover, the loading and coverage of cobalt and nickel on ZrP with different morphologies also affect the OER activity.<sup>19</sup> More recently, the confinement of nickel-iron mixtures in the interlayer environment of the ZrP layered structure has been found to stabilize Fe-rich compositions. The enhanced activity and stability of the resulting OER catalysts were primarily attributed to the species intercalated within the layers, rather than to those adsorbed on the surface.<sup>16</sup> The synthesis of zirconium phosphonates from phosphonic acids bearing amino acid functionalities has led to materials with structural arrangements and reactivity markedly different from those of conventional  $\alpha$ - and  $\gamma$ -type zirconium phosphonates.<sup>20</sup> In particular, zirconium phosphate phosphonates derived from N,N-bis(phosphonomethyl)phosphonic acids with branched structures, synthesized from glycine, 4-aminobutyric acid, 5-aminovaleric acid, and 6-aminocaproic acid, exhibit unique coordinative and exfoliation properties. These zirconium phosphate bis(phosphonomethyl)aminocarboxylates (ZPACs) display efficient interactions with cations and basic molecules due to the presence of exposed -COOH and P-OH groups on the layer surfaces.<sup>21,22</sup> Palladium and silver NPs were efficiently immobilized on ZPACs to obtain catalysts<sup>23-25</sup> and antibacterial materials.<sup>26,22</sup> Despite the growing interest in layered zirconium phosphate derivatives as hosts for transition metal species, their potential as chemically tunable hybrid platforms for stabilizing earth-abundant OER catalysts remains underexplored. In particular, the influence of organic phosphonate functionalization, interlayer organization, and exfoliation degree on metal



coordination and catalytic response has not been systematically investigated. In this paper, the coordination ability of ZPACs was exploited to immobilize  $\text{Fe}^{3+}$  and  $\text{Ni}^{2+}$  ions on previously exfoliated materials in order to prepare efficient and stable electrocatalysts for OER in alkaline media. The presence of exposed functional groups on the surfaces of the exfoliated ZPAC layers enabled strong interactions with Ni and Fe ions, promoting homogeneous dispersion and preventing aggregation of the active species. The structural flexibility, high ion-exchange capacity, and excellent dispersion characteristics of the exfoliated ZPAC materials allowed for the fine-tuning of the metal loading and the local coordination environment. These features contributed to increasing the electrochemically active surface area, improving the electron transfer kinetics, and enhancing the catalytic efficiency. By leveraging the unique structural and chemical properties of exfoliated ZPAC materials, we provided a promising route for the development of next generation OER catalysts based on earth-abundant transition metals, with potential implications for sustainable hydrogen production and energy conversion technologies.

## 2. Experimental section

### Materials

Zirconium oxychloride octahydrate ( $\text{ZrOCl}_2 \cdot 8\text{H}_2\text{O}$ , 98%) was obtained from Alfa Aesar. Multi-walled carbon nanotubes, iron(III) chloride ( $\text{FeCl}_3$ ), nickel(II) acetate tetrahydrate ( $\text{Ni}(\text{OCOCH}_3)_2 \cdot 4\text{H}_2\text{O}$ , 98%), Nafion<sup>TM</sup> 1100 perfluorinated resin solution (5wt%) and all other chemicals were purchased from Merck and used as received without any further purification.



## Synthesis of zirconium phosphate bis(phosphonomethyl)aminocarboxylates

View Article Online  
DOI: 10.1039/D6TA01464J

The N,N-bis(phosphonomethyl)aminocarboxylic acids with formula  $(\text{H}_2\text{O}_3\text{PCH}_2)_2\text{N}(\text{CH}_2)_n\text{COOH}$ , with  $n = 1, 3, 4,$  and  $5$ , (hereafter  $\text{H}_5\text{L}$ ) were synthesized by Moedritzer-Irani reaction<sup>27</sup> starting from the relative aminoacids (glycine for  $n=1$ , 4-aminobutyric acid for  $n=3$ , 5-aminovaleric acid for  $n=4$ , and 6-aminocaproic acid for  $n=5$ ), as reported in ref. 22. The synthesis of the corresponding zirconium phosphate bis(phosphonomethyl)aminocarboxylates with formula  $\text{Zr}_2(\text{PO}_4)_2\text{H}_5[(\text{O}_3\text{PCH}_2)_2\text{N}(\text{CH}_2)_n\text{COO}]_2 \cdot m\text{H}_2\text{O}$  (hereafter ZGLY for  $n = 1$ ; ZGABA for  $n = 3$ ; ZVAL for  $n = 4$ ; ZCAP for  $n = 5$ ; ZPAC in general) have been carried out following the method reported in Refs. 21,22. Briefly, 9 mmol of  $\text{H}_5\text{L}$  were solubilized in 93 mL of a suitable solvent (water for ZGLY, and ZGABA; 1:9 V/V propanol-water for ZVAL; 1:1 V/V propanol-water for ZCAP) and 6 mL of 1 M  $\text{H}_3\text{PO}_4$  was added to this solution ( $\text{H}_5\text{L}/\text{H}_3\text{PO}_4$  molar ratio = 1.5). A second solution was obtained by dissolving 1.93 g  $\text{ZrOCl}_2 \cdot 8\text{H}_2\text{O}$  (5.9 mmol) in 20.4 mL of 2.9 M HF (59 mmol; HF/ $\text{Zr}^{4+}$  molar ratio = 10). These solutions were mixed in a 500 mL Teflon bottle and put in an oven for three days at 90 °C. Then, the product was filtered and washed three times with water and dried in an oven at 60 °C. The calculated ion exchange capacity (IEC) for ZGLY, ZGABA, ZVAL and ZCAP is 3.8, 3.5, 3.4, and 3.3 mequiv/g, respectively.

### Preparation of NiFeZPAC catalysts

The metal-ZPACs, in the form of colloidal dispersions, were obtained after the exfoliation of ZPACs followed by direct ion exchange. First, 100 mg of ZPACs were suspended in 20 mL of water, and 0.1 M *n*-propylamine was added dropwise (1.2 mL for ZGLY; 1.1 mL for ZGABA; 1.0 mL for ZVAL; 1 mL for ZCAP; ZPAC/*n*-propylamine molar ratio of 1.1) under vigorous magnetic stirring. This mixture was stirred for at least one hour, up to complete



exfoliation and the formation of a stable colloidal dispersion of lamellae. To the ZGLY dispersion, volumes of 0.05 M Ni(OCOCH<sub>3</sub>)<sub>2</sub>·4H<sub>2</sub>O and 0.05 M FeCl<sub>3</sub>, previously mixed, were added dropwise in order to achieve the following Ni molar fractions ( $x_{Ni} = Ni(II)/(Ni(II)+Fe(III))$ ) 1, 0.85, 0.75, 0.25 and 0.10. As far as ZGABA, ZVAL, and ZCAP dispersions, they were treated with a solution containing a  $x_{Ni}$  equal to 0.75. After 24 hours under stirring, the products were recovered by centrifugation and washed three times with deionized water, and resuspended in 20 mL of deionized water. A known volume of each functionalized dispersion was dried to constant weight in an oven at 100 °C to determine the content of anhydrous metal-ZPAC in the dispersions. The content of metal-ZPAC in each dispersion was found to be 4 mg ml<sup>-1</sup>.

To determine the metal uptake, a fraction of the dispersion was recovered by centrifugation (5000 rpm for 15 min), dried in an oven at 100 °C, and analyzed by ICP upon acid digestion. The amount of salt solutions used is reported in Table 1 beside the amount of metal uptake expressed as  $x_{Ni}$  in the solid.

**Table 1.** Volumes of 0.05 M Ni(OCOCH<sub>3</sub>)<sub>2</sub>·4H<sub>2</sub>O and 0.05 M FeCl<sub>3</sub> used to prepare the NiFeZPAC catalysts,  $x_{Ni}$  in solution and in the solid as determined with ICP.

	Ni <sup>2+</sup> (mL)	Fe <sup>3+</sup> (mL)	Ni/(Fe+Ni) solution molar fraction	Ni/(Fe+Ni) solid molar fraction
NiZGLY	2.0	-	1	1
Ni <sub>0.89</sub> Fe <sub>0.11</sub> ZGLY	2.8	0.5	0.85	0.89
Ni <sub>0.68</sub> Fe <sub>0.32</sub> ZGLY	2.4	0.8	0.75	0.68
Ni <sub>0.48</sub> Fe <sub>0.52</sub> ZGLY	0.66	1.96	0.25	0.48
Ni <sub>0.40</sub> Fe <sub>0.60</sub> ZGLY	0.25	2.24	0.10	0.40
Ni <sub>0.79</sub> Fe <sub>0.21</sub> ZGABA	2.4	0.78	0.75	0.79
Ni <sub>0.78</sub> Fe <sub>0.22</sub> ZVAL	2.2	0.78	0.74	0.78
Ni <sub>0.77</sub> Fe <sub>0.23</sub> ZCAP	2.2	0.74	0.75	0.77



## Material characterization

View Article Online  
DOI: 10.1039/D6TA01464J

The amounts of iron, nickel, zirconium and phosphorus were obtained by inductively coupled plasma-optical emission spectrophotometry (ICP-OES) using a Varian Liberty Series II instrument working in axial geometry after the mineralization of samples with hydrofluoric acid and nitric acid. Field emission-scanning electron microscopy (FE-SEM) images were collected with a LEO 1525 ZEISS instrument working with an acceleration voltage of 15 kV. The elemental mapping of metals in samples was performed by using energy-dispersive X-ray spectroscopy (EDS). X-ray diffraction (XRD) patterns were collected with the Cu-K $\alpha$  radiation on a Bruker D8 Advance diffractometer and PW3050 goniometer, equipped with a Lynxeye XE-T detector. The long fine focus (LFF) ceramic tube was operated at 40 kV and 40 mA.

Attenuated total reflection (ATR) measurements were carried out with a Shimadzu IR-8000 spectrophotometer. The spectral range collected was 400 to 4000  $\text{cm}^{-1}$ , with a spectral resolution of 4  $\text{cm}^{-1}$ , acquiring 200 scans.

Raman spectra were acquired by using a WITec Raman alpha300RA confocal microscope (WITec, Ulm, Germany) equipped with a 532 nm excitation wavelength, 75 mW diode pump solid state laser. Samples deposited on FTO were directly placed on a microscopy glass specimen at room temperature. Spectra were acquired by accumulation of 80 scans at 1 s integration time in the Stokes range of 0-3600  $\text{cm}^{-1}$ . Spectra were processed by shape baseline subtraction at 150 size and cosmic ray removal. 2D scans were performed on a 60x60  $\mu\text{m}$  area at 100x100 pixel resolution and at 30 mW laser power fiber, using a Zeiss EC Epiplan-Neofluar Dic 100x / 0.9 objective. All scans and spectra were processed by the WITec Suite 7.0 software.

Scanning Transmission electron microscopy (STEM) High-Angle Annular Dark Field (HAADF) and Bright Field (BF) images were acquired using a TALOS F200X G2 (Thermo-



Fisher Scientific). This microscope is equipped with a high-brightness Field Emission Gun (X-FEG, 80–200 keV) and four in-column SDD Super-X detectors for Energy-dispersive X-ray spectroscopy (EDS), which was used to determine the distribution of nickel and iron ions on ZPACs.

X-ray photoelectron spectroscopy (XPS) analyses were performed using a Physical Electronics VersaProbe II spectrometer equipped with a monochromatic Al K $\alpha$  X-ray source ( $h\nu = 1486.6$  eV). Charge compensation was achieved using a dual-beam charge neutralizer operating at 100 W and 20 kV. All measurements were conducted under ultra-high vacuum conditions ( $\approx 10^{-7}$  Pa). The acquired spectra were fitted using PHI SmartSoft software and further processed with the MultiPak package (version 9.3). Binding energy calibration was carried out by referencing the C 1s peak of adventitious carbon to 284.8 eV, which was also used to correct for any charging-induced shifts.

### Electrochemical measurements

Electrochemical studies were performed using a Squidstat Solo potentiostat (Admiral Instruments) in a three-electrode configuration, employing a 3 mm diameter glassy carbon disk or a FTO as the working electrode, a platinum wire as the counter electrode, and a Hg/HgO (1 M NaOH) reference electrode. All measurements were carried out at room temperature using a 0.1 M KOH solution as electrolyte. All polarization curves were corrected for ohmic losses (iR-correction) using the solution resistance extracted from the high-frequency intercept of electrochemical impedance spectroscopy measurements.

Before use, the Hg/HgO electrode was calibrated against the reversible hydrogen electrode (RHE) by measuring the open-circuit potential (OCP) between a Pt/H<sub>2</sub> working electrode and the Hg/HgO reference electrode. Both electrodes were immersed in a 0.1 M KOH solution and the OCP was recorded over 10 minutes. This procedure was repeated three times, yielding



an average value of 0.888 V. Accordingly, all potentials reported in this study are referenced to the reversible hydrogen electrode (RHE) using the equation:  $E \text{ (V vs. RHE)} = E \text{ (V vs. Hg/HgO)} + 0.888 \text{ V}$ .<sup>7</sup> Cyclic voltammograms (CVs) were recorded with scan rates of 20 and 100 mV/s, whereas the linear sweep voltammetry (LSV) curves were recorded from 0.5 to 0.8 V with a scan rate of 5 mV s<sup>-1</sup>. The good operational stability over repeated cycling of ZPACs was assessed by evaluating the current decrease at 1.888 V vs RHE after 100 cycles from 0.888 to 1.888 V at 100 mV/s. Chronoamperometric measurements were performed using an FTO as the working electrode, a Pt wire counter electrode, and a Hg/HgO reference electrode in 0.1 M KOH. In a first set of experiments, a potential step from open circuit potential to 0.69 V vs. Hg/HgO was applied for 3 hrs (sampling interval: 5 s) to all four NiFeZPAC catalysts, serving as a preliminary stability screen across the series. Subsequently, a long-term stability test of 24 hrs was performed on the best-performing catalyst, applying the same potential and sampling conditions under continuous OER operation. The electrochemically active surface area (ECSA) was calculated using the fitted value of the double layer capacitance ( $C_{dl}$ ) by using the formula:  $ECSA = C_{dl}/C_s$ , in which  $C_s$  is the specific capacitance of the electrolyte, which was set to the value of 40  $\mu\text{F}/\text{cm}^2$ .<sup>28</sup>  $C_{dl}$  was determined by recording CVs at different scan rates (5 - 800 mV/s) in a non-Faradaic region and corresponds to one-half the slope of the linear fit of the capacitive current ( $D_i = i_a - i_c$ ) versus scan rate plot, where  $i_a$  and  $i_c$  represent the anodic and cathodic currents, respectively, measured at the same potential in the non-Faradaic region of the cyclic voltammogram (Figure S7-S10). The values of turnover frequency (TOF) were calculated by assuming that every active metal atom is involved in the catalysis (lower TOF limits were calculated):  $TOF = I / (4 * F * n)$ , where  $I$  is the measured current at a certain overpotential, the number 4 means 4 electrons per mole of O<sub>2</sub>,  $F$  is Faraday's constant (96500 C mol<sup>-1</sup>) and  $n$  is the number of moles of the total active metals on the substrate.<sup>29</sup> The Nyquist plots were acquired from electrochemical impedance



spectroscopy (EIS) measurements over a scanning frequency range of 100 kHz to 0.1 Hz at 0.01 V. Chronoamperometric measurements were performed using a FTO as the working electrode, a Pt wire counter electrode and an Hg/HgO reference electrode in 0.1 M KOH. A potential step from open circuit potential to 0.67 V vs Hg/HgO was applied for 24 hrs with a sampling interval of 5 s.

The electrocatalyst ink was prepared by mixing 500  $\mu\text{L}$  of metal-ZPAC dispersion ( $4 \text{ mg mL}^{-1}$ ), 1.5 mL of isopropanol, 1 mg of carbon nanotubes (CNTs) and 10  $\mu\text{L}$  of Nafion as a binder. The dispersion was sonicated for 30 minutes to obtain a homogeneous ink. For LSV and CV measurements, 10  $\mu\text{L}$  of the resulting suspension was dropped on the surface of a glassy carbon electrode and dried in air until the solvent evaporated. The catalyst concentration in the ink was  $1 \text{ mg mL}^{-1}$ , corresponding to a catalyst loading of approximately  $0.14 \text{ mg cm}^{-2}$  on the electrode surface (geometric area of  $0.0707 \text{ cm}^2$ ). For XRD, Raman and XPS analyses performed on ink samples before and after electrocatalytic tests, the working electrode was prepared by drop-casting 10  $\mu\text{L}$  of the catalyst ink onto FTO, followed by air drying.

### 3. Results and discussion

#### Synthesis and characterization of NiFeZPAC catalysts

ZPACs were synthesized by slow decomposition of Zr(IV) fluoro complexes in the presence of  $\text{H}_5\text{L}$  and phosphoric acid. All materials exhibited P/Zr and L/ $\text{PO}_4$  molar ratios close to 2.5 and 2, respectively, consistent with the general formula  $\text{Zr}_2(\text{PO}_4)\text{H}_5(\text{L})_2 \cdot m\text{H}_2\text{O}$ . Detailed crystallographic data for ZGLY, ZGABA and ZVAL have already been reported in Refs. 21,22 with the complete structural description. Here, the schematic structure of anhydrous ZGLY, as a representative member of ZPAC isorecticular compounds, is reported in Figure 1. The layer of ZPAC consists of two planes of Zr octahedra connected by tetradentate phosphate groups located in the inner part of the layer. The two  $\text{O}_3\text{PC}$  phosphonate tetrahedra of the



phosphonic acid complete the coordination of Zr in the outer part of the layer. The two phosphonate tetrahedra are not chemically equivalent; one is tridentate and the other is monodentate with a free OH group. In this arrangement, the aminocarboxylic tails face the interlayer region. In this way, acid groups such as -COOH and -POH are exposed on the surface. This results in a high ability to intercalate basic molecules via acid-base reactions and to exchange protons with metal cations. Furthermore, the intercalation of propylamine produces a rapid swelling of the layered structure due to the incoming of water inside the highly polar interlayer region, leading to the complete delamination of the material<sup>23</sup> and the formation of a stable colloidal dispersion of single or packets of a few lamellae. NiFeZPAC with varying metal compositions was prepared by mixing an aqueous colloidal dispersion of ZPAC with a solution of the metal salts with known molar fraction. The resulting dispersion was directly used to prepare the catalytic inks to be deposited on the glassy carbon electrode. The characterization of the materials was performed on the dried powders recovered from the colloidal dispersions. In terms of composition, it was observed that the Ni/(Fe+Ni) molar fraction in the solid is generally higher than the corresponding one in the feeding solution (see Table 1 columns 4 and 5), suggesting a high selectivity of the materials towards the divalent metal.<sup>30</sup> In addition, elemental analysis of the solids revealed the absence of propylamine, suggesting an ion-exchange reaction between propylammonium ions, formed during the treatment with propylamine, and the metal ions.

View Article Online  
DOI: 10.1039/D6TA01464J



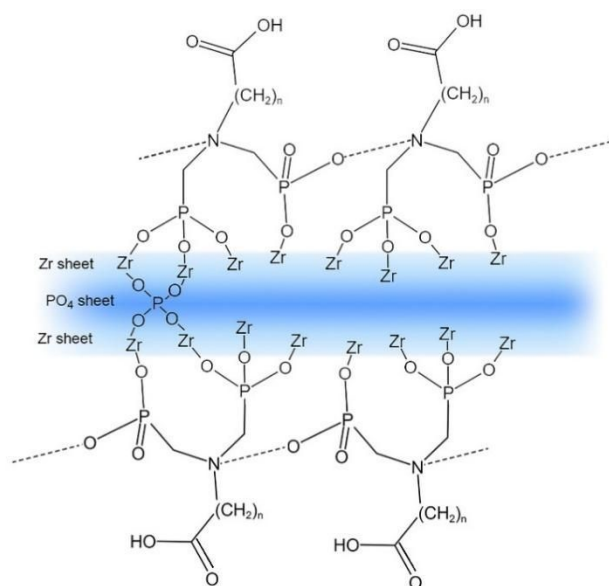


**Figure 1.** Schematic structure of anhydrous ZGLY.

NiFeZPAC powders were also analyzed by XRD and ATR and compared with the plain ZPACs and with the corresponding ink deposited on FTO glass. The XRD patterns of the  $\text{Ni}_{0.68}\text{Fe}_{0.32}\text{ZGLY}$  sample (Figure 2(a)) exhibited a shift of the first reflection towards lower 2 theta angles ( $4.96^\circ$ ) with respect to ZGLY ( $5.97^\circ$ ) due to the intercalation of metal ions in the interlayer region. In addition, the low intensity and the increased broadening of the first reflection indicate a loss of order along the layer stacking direction (crystallographic a-axis). NiFeZGLY samples with different Ni molar fractions ( $x_{\text{Ni}}=0.89; 0.48; 0.40$ ) showed the same modification of the X-Ray pattern (Figure S1). Thus, only a partial restacking of the layers of the exfoliated material was achieved in NiFeZGLY, leaving a degree of disorder and potentially a high exposed area. As far as ZGABA, ZVAL and ZCAP are concerned, the immobilization of  $\text{Ni}^{2+}$  and  $\text{Fe}^{3+}$  did not induce an increase in the interlayer distance (Figures 2(b)-(d)), probably due to the flexibility of the interlayer alkyl chains that can accommodate the metal ions in the free interlayer space available in these structures. The reflection intensities of NiFeZGABA are almost unchanged with respect to the original material, suggesting a reordering of the layers after the exchange of propylammonium with metal ions



(Figure 2(b)). A decrease in the intensity and an increase in the broadening of the first reflection of NiFeZVAL and NiFeZCAP are observed, indicating a certain degree of disorder, although less pronounced than that of NiFeZGLY (Figures 2 (c) and (d)). The XRD patterns of all the inks show reflections at low angles ascribable to the catalyst, confirming that its structure is retained in the ink.

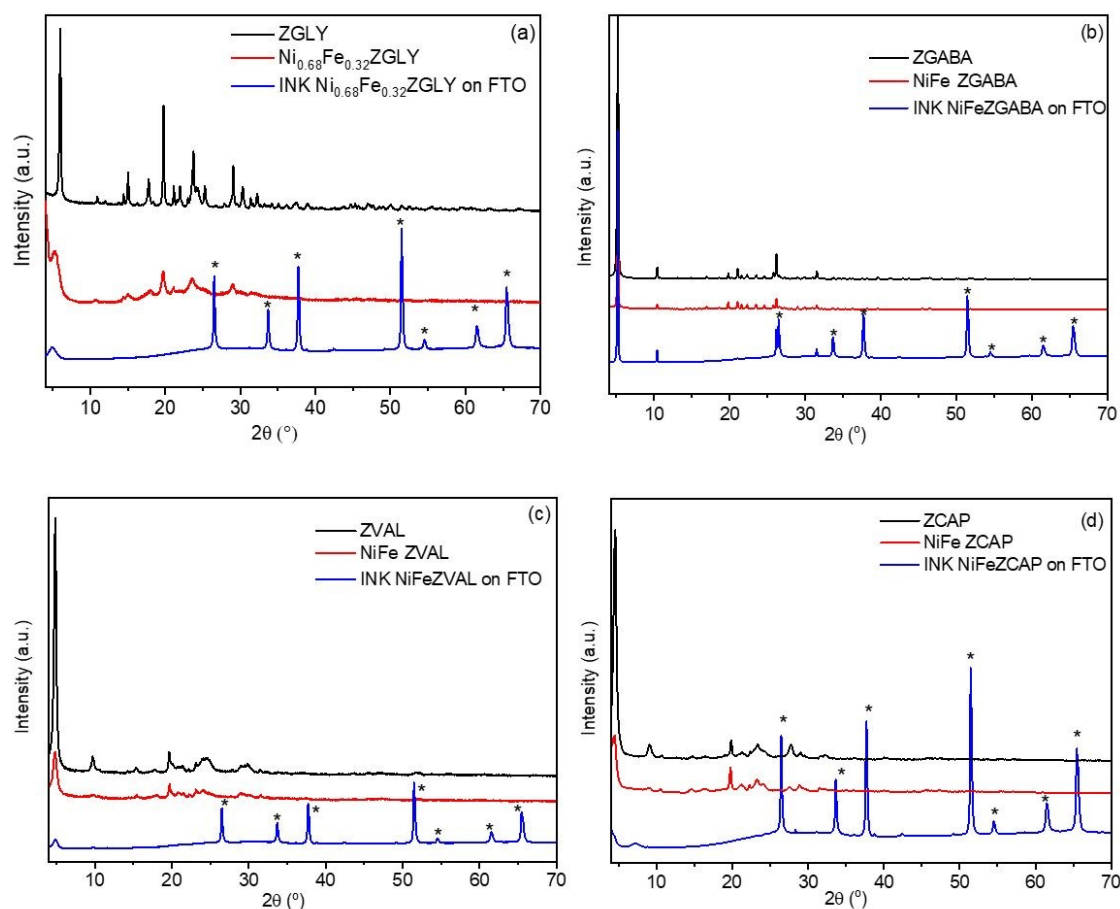


**Figure 2.** XRD pattern of NiFeZPACs and the corresponding inks deposited on FTO compared with the pristine ZGLY (ICSD No. 114801) (a), ZGABA (ICSD No. 115588) (b), ZVAL (ICSD No. 115589) (c), and ZCAP (d). \* indicates the reflections of FTO.

Figure 3 reports the ATR spectra of the NiFeZPACs in the 400-2000  $\text{cm}^{-1}$  region, alongside those of the starting materials for comparison. The bands in the range 1700-1750  $\text{cm}^{-1}$  of the pristine materials can be assigned to the asymmetric stretching of non-coordinated C=O and



to the stretching of the COOH groups involved in hydrogen bonds, as reported previously.<sup>22</sup> After the immobilization of metal cations in NiFeZPACs, the signals of COOH groups are totally or partially replaced by the asymmetric and symmetric stretching of COO<sup>-</sup> group at 1650-1550 cm<sup>-1</sup> and 1420 cm<sup>-1</sup>, suggesting the interaction of metal cations with the pendant carboxylic groups. In the ZPAC spectra, the band at about 960 cm<sup>-1</sup> is assigned to the  $\nu_1$  symmetric stretching vibrations of PO<sub>4</sub><sup>3-</sup>, the intense bands in the range 1020-1150 cm<sup>-1</sup> are attributed to the  $\nu_3$  antisymmetric stretching vibrations of PO<sub>4</sub><sup>3-</sup>, and the band at 1200 cm<sup>-1</sup> is due to the P=O stretch. These bands remain unchanged in NiFeZGABA, NiFeZVAL and NiFeZCAP, while they are shifted towards lower wavenumber in NiFeZGLY. This shift is indicative of different interactions of the phosphonic groups resulting from the exfoliation of the solid<sup>22</sup> and supports the XRD-based hypothesis that NiFeZGLY retains the high degree of disorder typical of colloidal dispersion. ATR spectroscopy shows a broader and weaker P-O peak compared to ZPACs, confirming a structural change and the presence of multiple P-O environments.

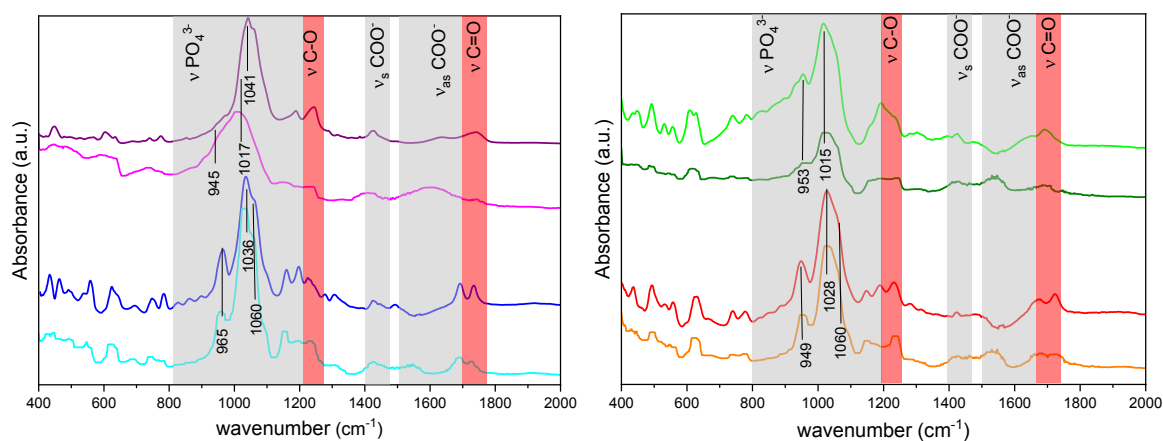


**Figure 3.** ATR spectra of ZGLY (purple line), Ni<sub>0.68</sub>Fe<sub>0.32</sub>ZGLY (magenta line); ZGABA (blue line), NiFeZGABA (cyan line); ZVAL (green line), NiFeZVAL (dark green line); ZCAP (red line), NiFeZCAP (orange line) in the spectral region: 400-2000 cm<sup>-1</sup>.



The surface of the catalysts in powder, was studied by XPS. The survey spectra, not shown here, display the presence of all the expected constituents elements. Tables S1 and S2 list the surface chemical composition in atomic concentration % and the P/Zr, Zr/N and C/N atomic ratios (nominal and found), respectively. As expected, the carbon content increases with increase of the length of the alkyl chain and concomitantly, the nitrogen content decreases.. The P/Zr atomic ratios are always slightly higher than the nominal values (2.5). This is explained since P is more external than Zr and XPS is a very surface sensitive technique. In a similar way, the Zr/N atomic ratios are always lower than the nominal values. Interestingly, the C/N found ratios are more or less similar to the nominal values. Therefore, XPS compositional analysis confirms the proposed composition. The high resolution C 1s core level spectra of the studied catalysts (Figure 4) can be decomposed into three contributions at 284.5-284.7 eV, 285.7-285.9 eV, and 288.1-288.3 eV that are assigned to adventitious carbon and -C-C- bonds the first contribution, to C-N, C-P, and C-COO bonds the second, and carboxylic the third. The high resolution N 1s spectra (Figure 4) show two contributions at 399.4-399.7 eV and 401.7 eV. The former is assigned to R<sub>3</sub>-N and the latter to R<sub>3</sub>-NH<sup>+</sup>. For the NiFeZCAP, NiFeZVAL, and NiFeZGABA samples, the spectra are dominated by the major peak corresponding to R<sub>3</sub>-NH<sup>+</sup> species. Conversely, in Ni<sub>0.68</sub>Fe<sub>0.32</sub>ZGLY the peak corresponding to R<sub>3</sub>-N shows a prominent increase in intensity. This suggests enhanced metal-nitrogen coordination, facilitated by the short alkyl chain of the GLY moieties which permits the simultaneous coordination of metal ions through both the carboxylic and nitrogen groups despite their lower basicity.<sup>31</sup> Interestingly, a clear trend is observed with the progressive elongation of the alkyl chain (from GLY to CAP), the relative contribution of the coordinated or free R<sub>3</sub>-N species systematically decreases, while the protonated R<sub>3</sub>-NH<sup>+</sup> signal becomes dominant. The high-resolution Fe 2p and Ni 2p core-level spectra are shown in Figure 4, and their respective binding energy (BE) values are summarized in Table S3. These spectra



display highly similar profiles and present a common trend: the Fe  $2p_{3/2}$  and Ni  $2p_{3/2}$  peaks appear at 710.1–709.5 eV and 855.4–855.7 eV, respectively, confirming the presence of Fe(III) and Ni(II). However, the BE values for Fe are shifted toward lower energies compared to FeCl<sub>3</sub> (711.3 eV) and lie close to those reported for Fe<sub>2</sub>O<sub>3</sub> and/or FeOOH (710.60–710.95 eV and 710.20–710.60 eV), suggesting an oxygen-rich coordination environment around Fe<sup>3+</sup> via the COO<sup>-</sup> groups of the frameworks.<sup>32</sup> Regarding nickel, its BE values are higher than that of NiO (854.3 eV) and closely resemble those of Ni species interacting with carboxylate and amino groups, such as in Ni(2-aminobenzoate)<sub>2</sub> (855.9 eV),<sup>31</sup> which aligns with the observations made for the N 1s region. The high-resolution O 1s core-level spectra exhibit a main signal at 531.2–531.6 eV, which is attributed to carboxylate groups overlapping with the lattice oxygen of the phosphate/phosphonate matrix. In some cases, a weak contribution at 532.8–532.9 eV is detected, originating from P-OH groups. Notably, lattice oxygen associated directly with Fe or Ni was not observed. The high-resolution P 2p core-level spectra display a single symmetric signal at 133.1–133.4 eV, typical of P(V) species in phosphate/phosphonate environments. Finally, the high-resolution Zr 3d core-level spectra present a well-resolved Zr  $3d_{5/2}$  - Zr  $3d_{3/2}$  doublet, with the Zr  $3d_{5/2}$  peak located at 183.1–183.3 eV, which is characteristic of zirconium phosphate/phosphonate frameworks.

View Article Online  
DOI: 10.1039/D6TA01464J



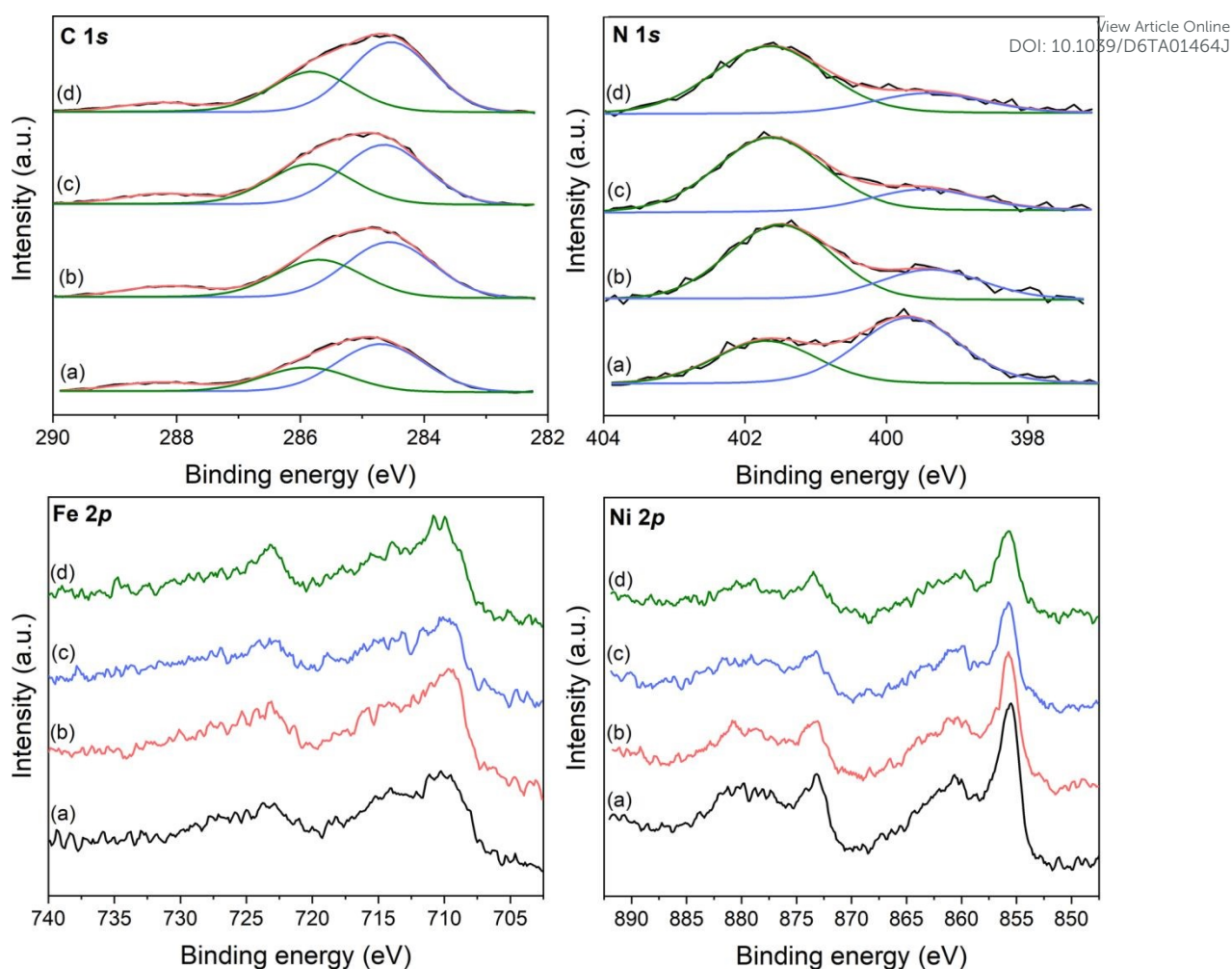


**Figure 4.** High resolution C 1s, N 1s, Fe 2p and Ni 2p core level spectra of Ni<sub>0.68</sub>Fe<sub>0.32</sub>ZGLY (a), NiFeZGABA (b), NiFeZVAL (c) and NiFeZCAP (d).

In order to investigate the distribution of the active metals on ZPACs, FE-SEM and EDS analyses were performed (Figure S2). Elemental mapping of Zr, Ni, and Fe shows that these elements are uniformly distributed throughout the whole materials confirming the immobilization of metal species on the particles.

To gain deeper insights at the nanoscale, the structural features of the NiFeZPAC samples were further investigated by STEM (Figure 5). The STEM-BF images confirm the formation of thin, exfoliated nanosheets without the presence of crystalline metal nanoparticles or segregated phases.



EDS reveals a homogeneous spatial distribution of Ni and Fe species across the nanosheets with no evidence of metal aggregation at the nanoscale. The uniform dispersion of metal ions within the hybrid framework supports the effectiveness of the amino acid-derived zirconium phosphate phosphonate structure in confining and stabilizing the precursors of the active species.

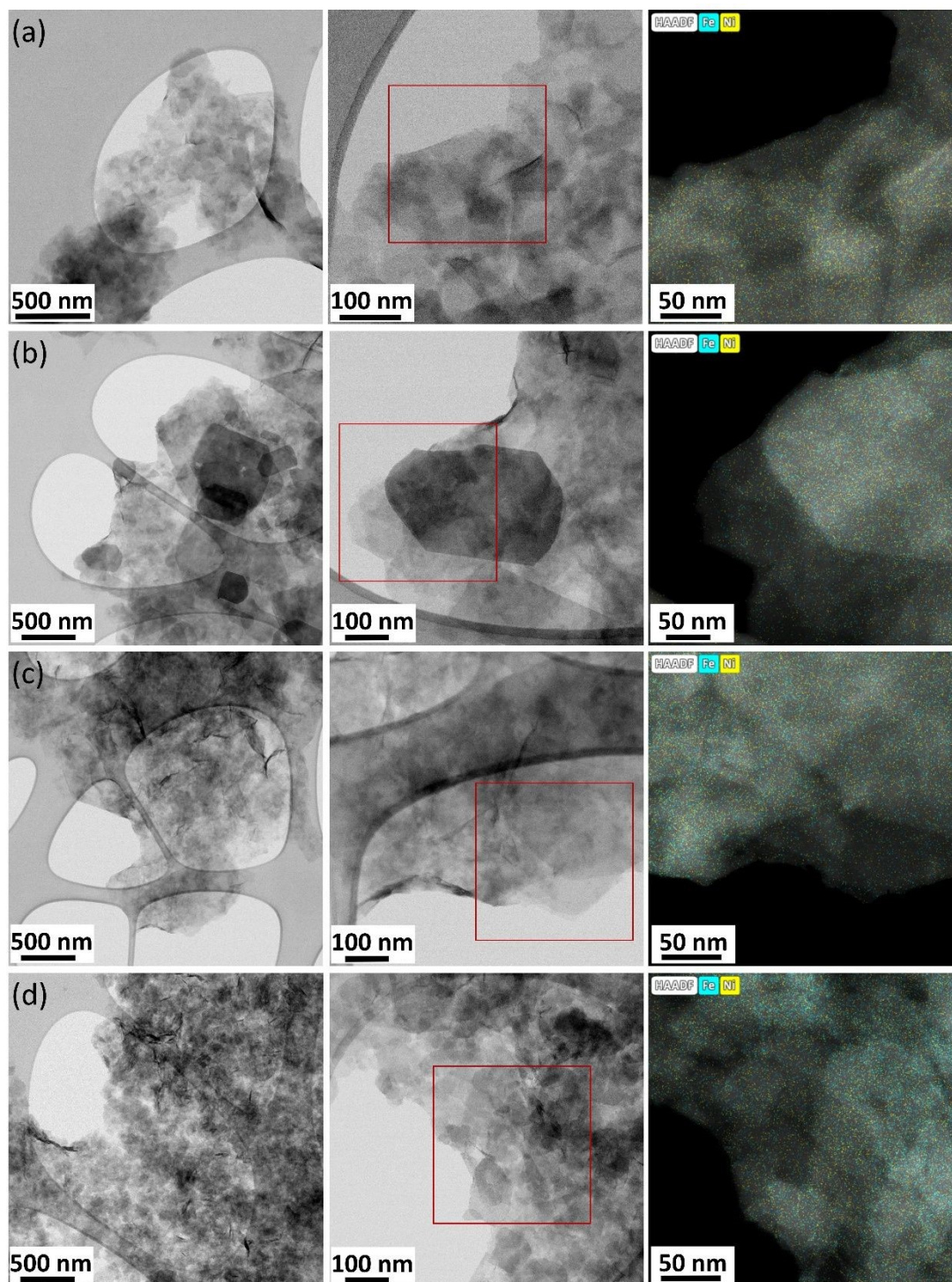


**Figure 5.** STEM-BF images at different magnifications of NiFeZPACs exfoliated nanosheets and EDS elemental mapping. EDS of Ni (yellow) and Fe (cyan) species within the hybrid framework.

All catalyst inks were characterized by SEM before electrochemical testing (Figures S3-S6). The images show that the as-deposited films consist of platelets horizontally oriented and partially fuse together, forming a nearly continuous film on the electrode surface. The morphology is not substantially altered by the addition of CNTs, and the catalysts appear well dispersed in the ink.

### Electrochemical measurements

Several studies have established the overpotential at a current density of  $10 \text{ mA cm}^{-2}$ , referenced to the geometric surface area of the electrode, as a standard metric for evaluating OER performance. Accordingly, the electrocatalytic activity of ZPACs was assessed by comparing their overpotential at  $10 \text{ mA cm}^{-2}$ . The electrocatalytic performance of the NiFeZPAC materials toward the oxygen evolution reaction was evaluated in alkaline media using cyclic voltammetry (CV) and linear sweep voltammetry (LSV). For consistency, the overpotential ( $\eta_{10}$ ) required to reach a geometric current density of  $10 \text{ mA cm}^{-2}$  was adopted as the primary benchmarking parameter. The  $\eta_{10}$  values for each catalytic system were obtained by averaging the measurements from the first CV of three independently prepared working electrodes. The metal-free ZPACs exhibit negligible OER activity within the investigated potential window, confirming that the zirconium phosphate–phosphonate framework acts as an electrochemically inert but structurally and chemically robust support. Notably, the incorporation of iron has been proven as an essential element in these high-efficiency catalysts. However, the best doping concentration of Fe is indicated as quite



controversial in the literature.<sup>33-35</sup> Therefore, initial studies were carried out on the system ZGLY in order to optimize the Ni/Fe ratio in terms of electrocatalytic performance. Figure 6 displays the cyclic voltammograms for the composites with varying Fe content. As expected, Ni-functionalized ZGLY show measurable OER activity, although with a relatively high overpotential of 596 mV (Figure 6) to achieve a geometric current density of 10 mA cm<sup>-2</sup>.

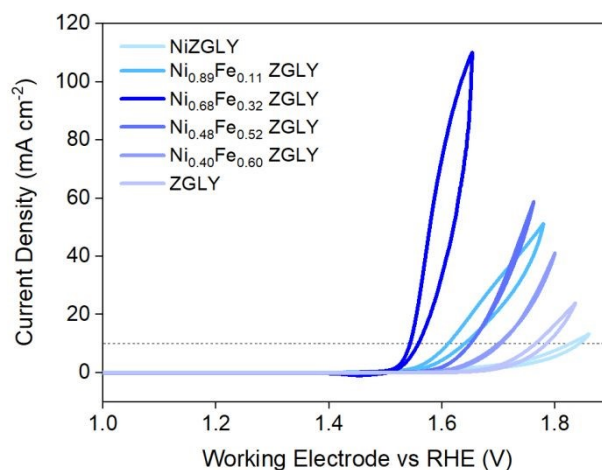


**Figure 6.** Cyclic voltammetry curves for all synthesized NiFeZGLY in 0.1 M KOH with a scan rate of 100 mV s<sup>-1</sup>. The CV curve of ZGLY was reported for comparison.

The incorporation of Fe markedly enhances the catalytic performance, in line with the well-established synergistic effect between Ni and Fe in alkaline OER catalysis.<sup>35</sup> Systematic variation of the Ni/Fe ratio in the ZGLY-based materials reveals a clear composition-dependent trend, with the lowest overpotential (304 mV) obtained for a Ni<sub>0.68</sub>Fe<sub>0.32</sub>ZGLY composition. Further increases in Fe content led to higher overpotentials, as seen for Ni<sub>0.48</sub>Fe<sub>0.52</sub>ZGLY (420 mV) and Ni<sub>0.40</sub>Fe<sub>0.60</sub>ZGLY (470 mV), indicating a decline in activity beyond the optimal composition (Figure 7A). These results highlight a synergistic effect between Ni and Fe within the zirconium phosphonate framework, where balanced metal incorporation enhances charge transfer and active site efficiency, while excessive Fe content diminishes the catalytic performance. The observed optimal composition is consistent with



literature reports on Ni-Fe (oxy)hydroxide systems,<sup>35</sup> while emphasizing the role of the zirconium phosphonate framework in stabilizing an efficient interfacial arrangement of the two metals. Further insight into the reaction kinetics is provided by Tafel analysis derived from LSV measurements (Figure 7B). The Tafel slope decreases significantly upon Fe incorporation, reaching a minimum value of approximately 32.9 mV dec<sup>-1</sup> for Ni<sub>0.68</sub>Fe<sub>0.32</sub>ZGLY. This low slope is indicative of fast reaction kinetics and suggests that the rate-determining step is effectively facilitated by the cooperative interaction between Ni and Fe centers confined at the interface. At higher Fe contents, the increase in Tafel slope reflects the decline in catalytic activity, reinforcing the existence of an optimal metal ratio for efficient catalysis.

Based on these findings, catalysts incorporating longer carbon chains were synthesized using an iron concentration corresponding to the optimized value identified for the ZGLY system.

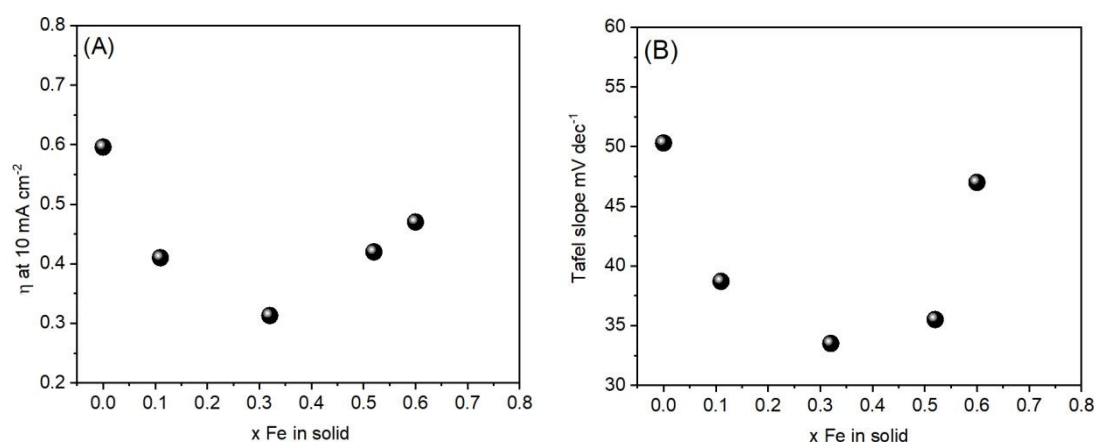


**Figure 7.** Overpotential of NiFeZGLY required for a current density of 10 mA cm<sup>-2</sup> in 0.1 M KOH (A) and Tafel slope (B) as a function of the Fe molar fraction (x) in the catalyst.

The cyclic voltammograms of the resulting NiFeZPACs are shown in Figure 8, with the corresponding overpotentials at 10 mA cm<sup>-2</sup> summarized in Table 2.

A comparison among NiFeZPACs derived from different amino acid ligands reveals that all systems exhibit relatively similar overpotentials (304-332 mV). The OER activities of these



different ZPACs confirmed the powerful synergy between the Ni and Fe active sites present on the catalyst surface.

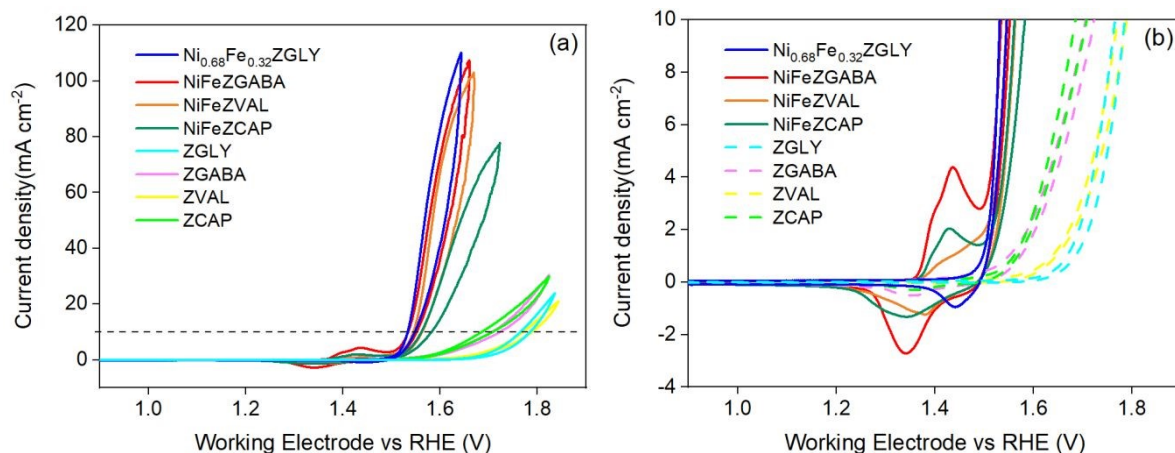


**Figure 8.** Cyclic voltammetry curves for all synthesized NiFeZPACs in 0.1 M KOH with a scan rate of  $100 \text{ mV s}^{-1}$ . Cyclic voltammetry curves for ZPACs were added for comparison (a). Enlargement of the CV curves in the current density range:  $-4$  and  $10 \text{ mA cm}^{-2}$  (b).

**Table 2.** Experimental overpotentials of NiFeZPACs obtained at  $j = 10 \text{ mA cm}^{-2}$ .

Sample	$\eta_{10}$ (mV)
$\text{Ni}_{0.68}\text{Fe}_{0.32}\text{ZGLY}$	304
NiFeZGABA	305
NiFeZVAL	315
NiFeZCAP	332

The cyclic voltammograms also display characteristic precatalytic redox features associated with the  $\text{Ni}^{2+}/\text{Ni}^{3+}$  transformation, commonly attributed to the  $\text{Ni}(\text{OH})_2/\text{NiOOH}$  redox couple in alkaline electrolytes. For NiFeZGABA, NiFeZVAL and NiFeZCAP, this redox process is clearly observed, whereas it is less distinct for NiFeZGLY. This behavior can be attributed to the higher OER current density in NiFeZGLY, which hides the redox signal and suggests an



earlier onset of catalytically active NiOOH species. As previously reported, increasing Fe content in Ni-Fe systems is commonly associated with a shift of the Ni<sup>2+</sup>/Ni<sup>3+</sup> redox couple toward higher potentials. At sufficiently high Fe concentrations, the redox feature becomes indistinguishable, coinciding with the sharp onset of the OER current and thereby no longer detectable in the voltammograms. This observation supports the idea that Fe modifies the electronic structure of Ni centers and promotes the formation of highly active NiOOH-type species during electrochemical operation.<sup>35</sup>

Tafel plots for each system were derived from LSV measurements (Figure 9 (a)), and representative curves are shown in Figure 9 (b).

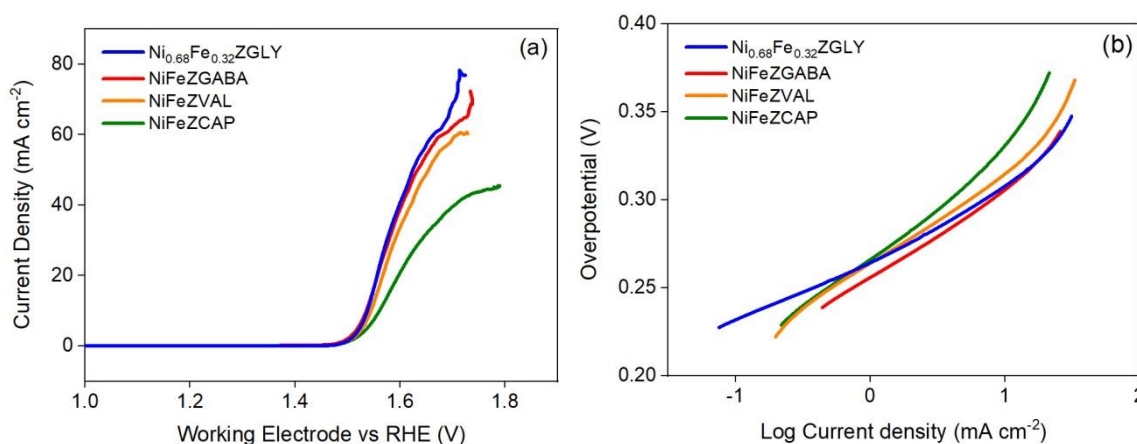


**Figure 9.** Linear sweep voltammograms of Ni<sub>0.68</sub>Fe<sub>0.32</sub>ZGLY, NiFeZGABA, NiFeZVAL, NiFeZCAP catalysts (a) and Tafel plots for NiFeZPAC-based catalysts (b).

The Tafel slopes of the NiFeZPAC catalysts fall within a narrow range of 32.9 to 52 mV dec<sup>-1</sup> (Table 3), indicating comparable intrinsic catalytic kinetics. These values are comparable to those reported for Ni<sub>1-x</sub>Fe<sub>x</sub>OOH thin films,<sup>28</sup> suggesting a similar mechanism for the OER in all systems.



**Table 3.** Tafel slope values of NiFeZPACs.View Article Online  
DOI: 10.1039/D6TA01464J

Sample	Tafel slope (mV dec <sup>-1</sup> )
Ni <sub>0.68</sub> Fe <sub>0.32</sub> ZGLY	32.9
NiFeZGABA	45.8
NiFeZVAL	48.0
NiFeZCAP	52.0

To place the performance of the NiFeZPAC catalysts in a broader context, their OER activity was benchmarked against representative state of the art Ni-Fe based electrocatalysts reported in the literature (Table S4). As shown, the optimized Ni<sub>0.68</sub>Fe<sub>0.32</sub>ZGLY catalyst exhibits an overpotential of approximately 304 mV at a geometric current density of 10 mA cm<sup>-2</sup>, which is slightly higher than that of widely studied hybrid systems operating in alkaline media. The corresponding Tafel slope of 32.9 mV dec<sup>-1</sup> falls within the lower range reported for highly active Ni-Fe based catalysts, indicating favorable reaction kinetics.

To comprehensively evaluate the electrocatalytic performance of the NiFeZPACs, several key parameters were analyzed, including ECSA, roughness factor (RF) and TOF. ECSA was estimated from the double-layer capacitance ( $C_{dl}$ ) measured via CV in the non-Faradaic region (Figures S7-S10) and normalized by a standard specific capacitance of 40  $\mu\text{F cm}^{-2}$ .<sup>28</sup> The ECSA values of the NiFeZPAC catalysts are comparable across the series (Table 4), indicating that the observed differences in OER activity cannot be ascribed to variations in electrochemically accessible surface area. Instead, the enhanced performance of selected compositions reflects differences in the nature, accessibility, and local coordination environment of the interfacial Ni-Fe active sites. These results highlight that chemical confinement within the zirconium phosphate phosphonate framework governs the effectiveness of Ni-Fe interactions and plays a key role in dictating OER activity.



Based on a geometric electrode area of  $0.0707 \text{ cm}^2$ , the RF of the NiFeZPAC catalysts were calculated to fall in the range of 8.21-11.89 (Table 4). These relatively low roughness factors are consistent with the planar morphology of the ZPAC structures. As observed in the SEM images (Figures S3-S6), the exfoliated nanosheets tend to align predominantly parallel to the substrate during ink deposition, which limits surface corrugation and results in modest roughness values.

**Table 4.** ECSA, RF and TOF @  $\eta = 350 \text{ mV}$  for NiFeZPACs.

Sample	ECSA ( $\text{cm}^2$ )	RF	TOF ( $\text{s}^{-1}$ )
Ni <sub>0.68</sub> Fe <sub>0.32</sub> ZGLY	0.68	9.62	0.047
NiFeZGABA	0.56	8.21	0.035
NiFeZVAL	0.84	11.89	0.029
NiFeZCAP	0.66	9.34	0.017

The TOF of the ZPAC catalysts ranges from  $0.047$  to  $0.017 \text{ s}^{-1}$  at an overpotential of  $350 \text{ mV}$ , with the highest and lowest values observed for the NiFeZGLY and NiFeZCAP, respectively, assuming that all metal atoms drop-casted onto the glassy carbon electrode participate in the OER. As commonly encountered for heterogeneous Ni-Fe-based OER catalysts, this assumption likely leads to an underestimation of the intrinsic activity, since only a fraction of the metal centers is expected to be electrochemically accessible under operating conditions. Accordingly, the reported TOF values should be regarded as apparent, lower-bound estimates that are primarily meaningful for comparative analysis within the ZPAC series rather than as absolute intrinsic metrics. The TOF values obtained in this work fall within the range reported for representative Ni-based and Ni-Fe-based OER catalysts, as well as benchmark IrOx systems (Table S5). It should be noted that literature TOF values are often derived using different assumptions regarding the number of active sites, and therefore the comparison is



primarily qualitative.<sup>36</sup> Notably, the relatively narrow TOF range among the NiFeZGLY, NiFeZGABA and NiFeZVAL is consistent with their comparable overpotential values (304-315 mV at 10 mA cm<sup>-2</sup>) and with the EIS results, which reveal moderate but limited variations in the charge-transfer resistance ( $R_{ct}$ ), with values ranging from 48 to 67  $\Omega$  (Figure S11). In contrast, the lower TOF observed for the ZCAP-based catalyst correlates with its higher overpotential (332 mV), suggesting a reduced utilization of active Ni-Fe sites rather than a fundamentally different active-site chemistry.

In order to investigate the intrinsic performance of these catalytic systems, the mass-normalized activities at an OER overpotential of 350 mV were calculated for ZPAC catalysts, taking into account the Ni loading in the amount of catalyst used, determined from ICP-OES measurements. Mass activity provides a practical metric of catalyst efficiency by normalizing the OER current to the catalyst mass, thereby reflecting the effective utilization of active species within the material. The mass activity of the NiFeZPAC catalysts shows a clear decreasing trend from the NiFeZGLY to the NiFeZCAP, with values of 4328, 3215, 2726, and 1592 A g<sup>-1</sup>, respectively, evaluated at the same overpotential. This trend closely reflects the behavior observed for the apparent TOF and overpotential values offering the additional advantage of a chemically tunable hybrid framework enabling controlled metal confinement. The higher mass activity of the NiFeZGLY can be attributed to its higher degree of exfoliation and structural disorder, which enhances catalyst dispersion and accessibility of electrochemically active sites. In contrast, the significantly lower mass activity observed for the NiFeZCAP is consistent with its higher overpotential and reduced TOF, suggesting limitations in active-site accessibility and interfacial exposure. Overall, the results highlight that catalytic performance is not solely governed by surface area or morphology, but is strongly influenced by the chemical environment and confinement of the active species within the hybrid framework.



**Table 5.** Ni loading in the ink,  $j$  @  $\eta=350$  mV, mass activity @  $\eta = 350$  mV.View Article Online  
DOI: 10.1039/D6TA01464J

Sample	Ni ( $\mu\text{g}$ )	$j_{350}$ ( $\text{mA cm}^{-2}$ )	M.A. <sub>350</sub> ( $\text{A g}^{-1}$ )
Ni <sub>0.68</sub> Fe <sub>0.32</sub> ZGLY	7.49	32.4	4328
NiFeZGABA	9.52	30.6	3215
NiFeZVAL	9.58	26.1	2725
NiFeZCAP	9.68	15.4	1591

To assess the stability of the catalyst under operating conditions, the CV analysis was repeated on the material after 100 cycles. As shown in Figure 10, the comparison between the first and the 100<sup>th</sup> cyclic voltammograms recorded in 0.1 M KOH reveals only minor changes in the overall voltammetric response for the NiFeZPAC catalysts. In particular, the samples exhibit a largely preserved current profile after repeated cycling, indicating good electrochemical robustness of the interfacial Ni-Fe sites under alkaline conditions.

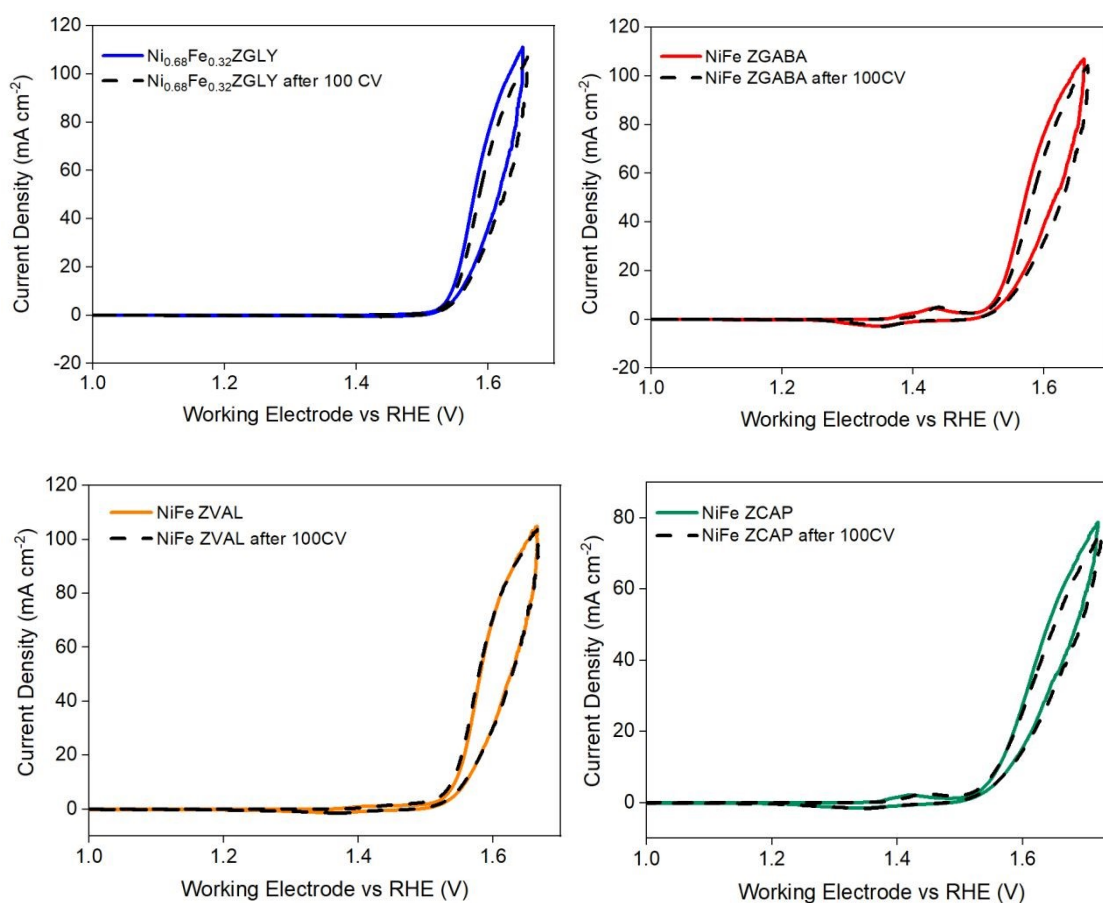


**Figure 10.** Comparison of the 1<sup>st</sup> (colored line) and 100<sup>th</sup> (black dashed line) cyclic voltammogram of NiFeZPACs recorded in 0.1 M KOH at a scan rate of 100 mV s<sup>-1</sup>. View Article Online  
DOI: 10.1039/D6TA01464J

In order to study the structural stability of the catalysts after electrochemical measurements by XRD analysis, the inks were deposited on an FTO electrode and the electrochemical tests were repeated (Figure 11). Notably, the catalytic performances were not affected by the support used. After electrochemical treatment in 0.1 M KOH for 100 cycles, no structural changes were observed. The patterns are primarily characterized by diffraction peaks arising from the FTO substrate, while only weak reflections attributable to the catalyst are detected at low  $2\theta$  values, consistent with the presence of the layered solids. The low intensity of the catalyst reflections suggests a low loading and/or high degree of exfoliation of the active phase on the FTO surface, with no evidence of additional crystalline impurities. Additionally, EDS elemental mapping confirms a uniform distribution of Ni and Fe within the ZPAC layers, after treatment with 0.1 M KOH solution and following 100 cycles of cyclic voltammetry (Figures S3-S6).

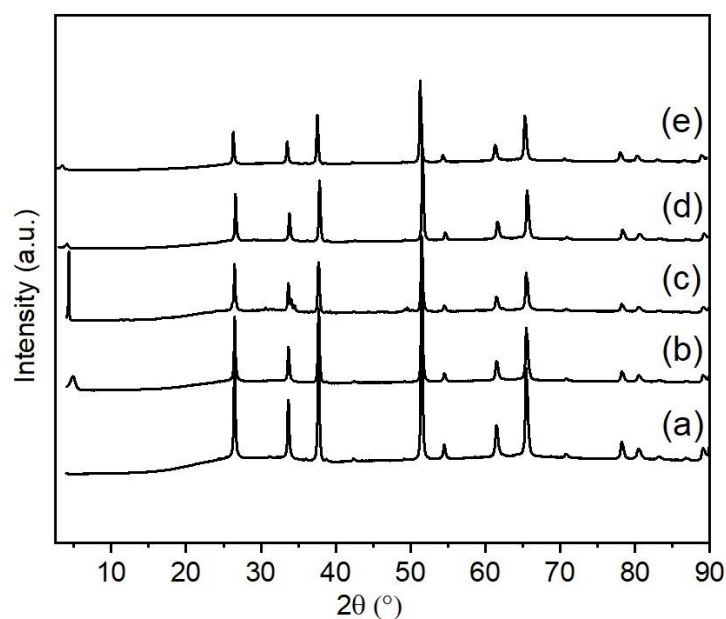


**Figure 11.** XRD patterns of NiFeZPACs on FTO after 100 CV. (a) FTO, (b) Ni<sub>0.68</sub>Fe<sub>0.32</sub>ZGLY, (c) NiFeZGABA, (d) NiFeZVAL and (e) NiFeZCAP.

Raman and XPS spectroscopies were employed to investigate the structural evolution of the NiFeZPAC inks deposited on an FTO electrode, induced by the electrochemical treatment. Figure 12 compares the Raman spectra collected before and after the reaction. The overlaid spectra clearly highlight the formation of new active phases following electrochemical conditioning. The most pronounced modifications occur in the 400-700 cm<sup>-1</sup> region, where the appearance of a band at  $\approx 460$  cm<sup>-1</sup> and the progressive definition of features in the 520-650 cm<sup>-1</sup> range are observed after reaction. These bands are attributable to NiOOH-type vibrations (notably the characteristic  $\approx 460$  cm<sup>-1</sup> mode) and Fe oxide/oxyhydroxide species, indicating partial oxidation of Ni<sup>2+</sup> to NiOOH and the concurrent formation of Fe-based oxyhydroxides during electrochemical operation, in agreement with previous reports on Ni-Fe electrocatalysts. The relative intensity of the NiOOH- and Fe-related bands differs among NiFeZGLY, NiFeZGABA, NiFeZVAL and NiFeZCAP, suggesting that the ligand environment modulates the extent of surface reconstruction of the electrochemically generated active phase. The insets in Figure 12 display representative post-reaction 2D Raman maps. The combined colour maps (red = CNTs; green = NiOOH/Fe oxide-oxyhydroxide species) reveal a heterogeneous but well-dispersed distribution of the oxidized Ni-Fe domains across the carbon network. Although all samples undergo surface activation consistent with electrocatalytic oxidation, clear differences in the spatial distribution and relative abundance of NiOOH and Fe oxide/oxyhydroxide species are observed, reflecting variations in composition and structure arising from the different ligands. These results support a correlation between the redox behaviour, the spectroscopic signature of the NiOOH-type phase in the ZPAC electrocatalysts, and their OER activity.<sup>35</sup>



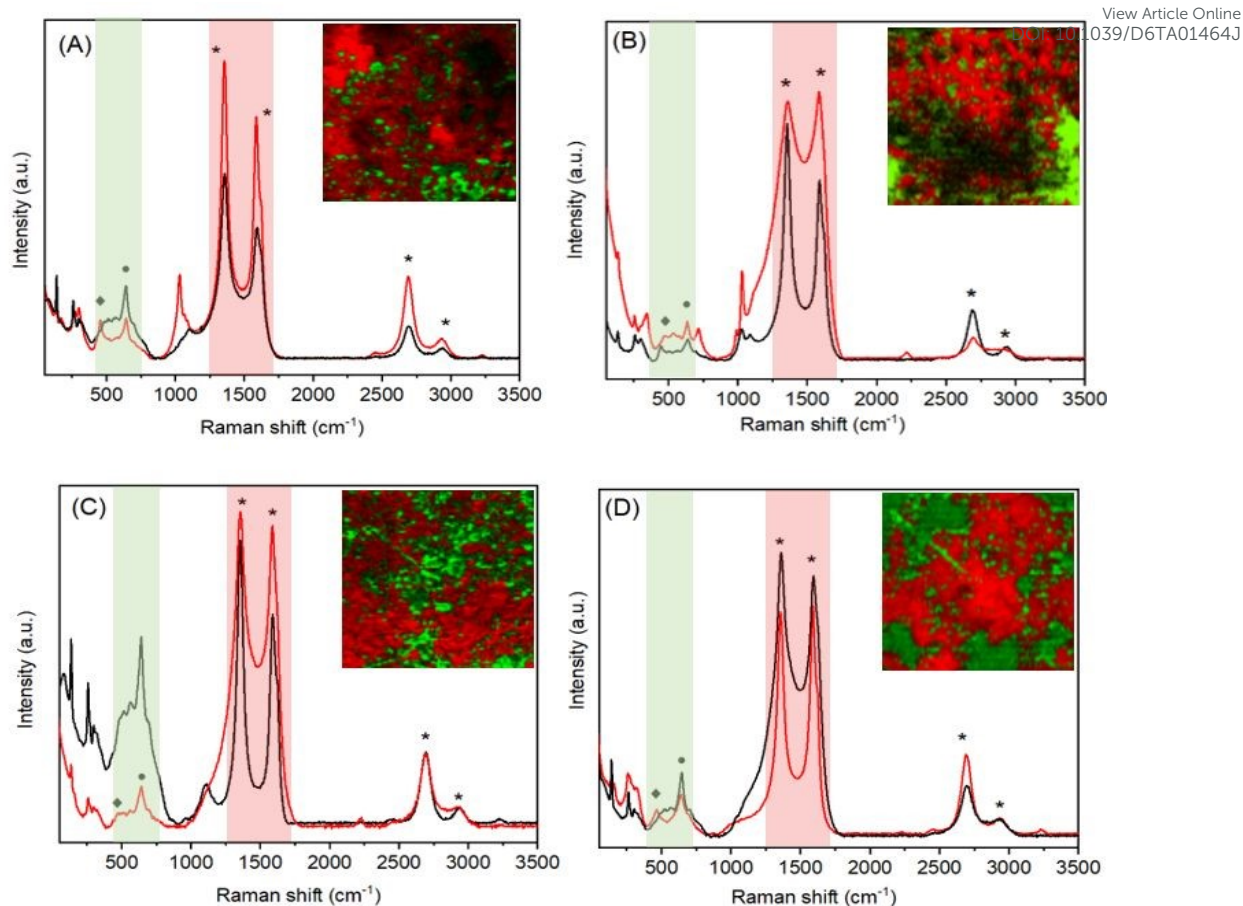


**Figure 12.** Raman spectra recorded before (black line) and after (red line) the electrochemical reaction for (A) NiFeZGLY, (B) NiFeZGABA, (C) NiFeZVAL, and (D) NiFeZCAP. Asterisks (\*) indicate bands attributable to CNTs; diamonds (◆) denote NiOOH-type vibrational modes; circles (●) mark Fe oxide/oxyhydroxide vibrations. Insets show representative Raman 2D maps collected after the reaction. Combined color maps are reported for NiFeZPACs where CNTs are shown in red and NiOOH/Fe oxide–oxyhydroxide species formed after the reaction are shown in green.

The interpretation of the XPS spectra is somewhat complicated by the high fluorine content originating from the Nafion binder. Specifically, the  $F_{KLL}$  Auger signal (859.0 eV) overlaps with the high-resolution Ni  $2p$  core level spectra (Figure 13). This spectral overlap is more pronounced for the inks formulated with NiFeZGABA and Ni<sub>0.68</sub>Fe<sub>0.32</sub>ZGLY, which exhibit



higher fluorine concentrations (Table S6). Nonetheless, the Ni 2  $p_{3/2}$  peak displays a new contribution or a shift toward higher binding energies compared to the pristine catalysts (Figure 13). These binding energy values are centered at 856.1–856.2 eV for NiFeZGABA, NiFeZVAL, and NiFeZCAP. Conversely, for the NiFeZGLY ink, only a high-energy shoulder is discerned. The appearance of this peak component at 856.2 eV is indicative of the formation of NiOOH species<sup>37</sup> in agreement with the complementary Raman spectroscopy findings. The high-resolution Fe 2 $p$  core-level spectra exhibit a relatively low signal-to-noise ratio due to the low iron content within the samples, making the precise identification of the Fe 2 $p_{3/2}$  peak position challenging. Nevertheless, for the ink based on NiFeZVAL and NiFeZCAP, distinct peak maxima are observed at 710.5 eV and 710.6 eV, respectively, which can be confidently ascribed to FeOOH species.<sup>32</sup> The structural transformations, observed via Raman and XPS spectroscopy, suggest an electrochemically driven surface reconstruction that promotes the in situ growth of active FeOOH/NiOOH phases, directly contributing to the enhanced electrocatalytic performance.

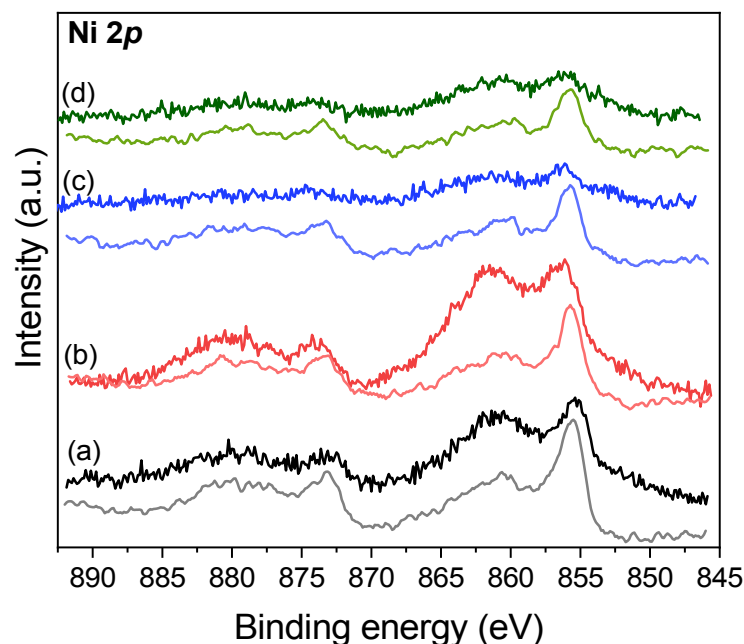


**Figure 13.** High resolution Ni 2*p* core level spectra of Ni<sub>0.68</sub>Fe<sub>0.32</sub>ZGLY (a), NiFeZGABA (b), NiFeZVAL (c) and NiFeZCAP (d), before (light color) and after (dark color) the electrochemical tests.

Operational stability is an important parameter for evaluating the practical applicability of electrocatalysts toward the oxygen evolution reaction. The electrochemical robustness of the NiFeZPAC catalysts was therefore further evaluated by chronoamperometric measurements in 0.1 M KOH, in which each catalyst was held at the potential required to sustain a current density of 10 mA cm<sup>-2</sup> while monitoring the current response over time. As shown in Figure 14, the Ni<sub>0.68</sub>Fe<sub>0.32</sub>ZGLY catalyst maintains a nearly constant current density during the measurement, indicating superior operational stability compared to the other members of the series. In contrast, zirconium phosphonates bearing longer alkyl chains exhibit a gradual decrease in current, suggesting a less stable interfacial configuration under alkaline OER conditions. The present results highlight the critical role of ligand structure and interfacial accessibility in determining both catalytic activity and operational stability within the ZPAC series.

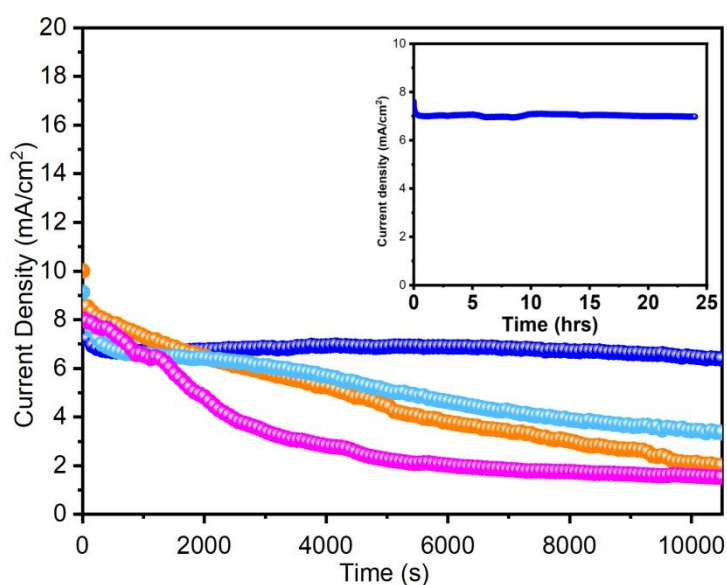


**Figure 14.** Chronoamperometric data of: Ni<sub>0.68</sub>Fe<sub>0.32</sub>ZGLY (blue line), NiFeZGABA (orange line), NiFeZVAL (light blue line), NiFeZCAP (pink line). The inset shows the long-term chronoamperometric stability test of Ni<sub>0.68</sub>Fe<sub>0.32</sub>ZGLY over 24 hrs.

Building on these observations, the long-term stability of the most promising sample, Ni<sub>0.68</sub>Fe<sub>0.32</sub>ZGLY, was further evaluated by chronoamperometry over 24 hrs under continuous OER operation (Figure 14, inset). An initial decrease in current density is observed within the first minutes, which can be attributed to surface restructuring and activation processes commonly reported for Ni–Fe-based catalysts. After this initial stage, the current density stabilizes and remains nearly constant over the entire duration of the test, with negligible loss of activity, confirming the excellent electrochemical durability of the catalyst under alkaline conditions. The sustained performance suggests that the zirconium phosphate–phosphonate framework effectively stabilizes the catalytically active species and prevents their aggregation or deactivation during prolonged operation. While the present results demonstrate good durability under laboratory conditions, extended testing under practically relevant conditions remains an important objective for future studies. To further assess the structural and chemical integrity of Ni<sub>0.68</sub>Fe<sub>0.32</sub>ZGLY under prolonged operating conditions, post-operando characterization was performed after the 24 hrs chronoamperometric test. XRD patterns collected after extended operation are indistinguishable from those obtained after 100 CV cycles, with no new crystalline phases and full retention of the low-angle reflections characteristic of the layered ZPAC scaffold (Figure S12). Raman spectra recorded after 24 hrs operation are fully consistent with those obtained after cycling, with the NiOOH band at ~460 cm<sup>-1</sup> and the Fe-oxyhydroxide features in the 520–650 cm<sup>-1</sup> region unchanged in position and relative intensity (Figure S12), confirming that the active oxyhydroxide phase reaches a stable chemical state during the initial activation transient and does not evolve



further under sustained OER conditions. SEM images confirm that the film retains its platelet-like morphology with no evidence of agglomeration or dissolution and EDS elemental mapping demonstrates a uniform spatial distribution of Ni, Fe, Zr, and P, ruling out metal leaching or phase segregation (Figure S13). Taken together, these results demonstrate that the ZPAC framework acts as a chemically robust host that confines and stabilizes the catalytically active NiOOH/FeOOH species, preventing the aggregation and deactivation that commonly limit the long-term performance of unsupported Ni–Fe electrocatalysts.

#### 4. Conclusion

This study demonstrates that amino acid-derived zirconium phosphate phosphonates constitute an effective and chemically versatile platform for the rational design of interface-confined Ni-Fe active sites for the alkaline oxygen evolution reaction. Controlled exfoliation of the layered zirconium phosphonate framework enables homogeneous immobilization of Ni<sup>2+</sup> and Fe<sup>3+</sup> ions at organic-inorganic interfaces, allowing precise tuning of metal composition, coordination environment, and accessibility of catalytically active sites. Systematic variation of the Ni/Fe ratio reveals a clear composition-performance relationship, with the optimized Ni<sub>0.68</sub>Fe<sub>0.32</sub>ZGLY catalyst delivering competitive OER activity, characterized by an overpotential of approximately 304 mV at 10 mA cm<sup>-2</sup> and a low Tafel slope of 32.9 mV dec<sup>-1</sup>. While these values are comparable to those of state of the art Ni-Fe-based electrocatalysts, the present system distinguishes itself through the use of a chemically robust zirconium phosphonate framework that provides well-defined interfacial confinement and enhanced structural stability under alkaline conditions. Among the investigated materials, the glycine-derived zirconium phosphonate exhibits superior mass activity and electrochemical robustness, which can be attributed to its higher degree of exfoliation and the persistence of structural disorder, maximizing interfacial exposure of Ni-Fe active species.



Post-operando Raman spectroscopy and XPS identify the in situ formation of NiOOH and FeOOH as the principal catalytically active phases, which are effectively stabilized by the zirconium phosphonate framework, mitigating aggregation and structural degradation under alkaline conditions. Crucially, the ZPAC framework suppresses the aggregation and deactivation of these transient phases, as confirmed by structural analyses after 100 CV cycles. The highest stability was displayed by Ni<sub>0.68</sub>Fe<sub>0.32</sub>ZGLY, which, after 24 hrs of chronoamperometry at 10 mA cm<sup>-2</sup>, confirmed the full retention of framework integrity and uniform metal distribution. Taken together, these results reframe the role of the ZPAC host: rather than a passive support, it functions as an active chemical environment that stabilizes transient oxyhydroxide phases, tunes their nucleation density and controls their long-term persistence under alkaline operation. This work establishes interfacial confinement within exfoliated, organically functionalized zirconium phosphonate layers as a general and transferable strategy for designing durable, earth-abundant OER electrocatalysts, with straightforward extension to other first-row transition metal combinations and to the broader class of multi-electron electrochemical energy conversion reactions.

### Author Contributions

A.D., M.N.: Conceptualization, methodology, supervision, data curation, writing&original draft, writing&review and editing. I.D.: Investigation, data curation, G.M.R., R.V.: data curation and writing&review and editing. S.G.: Investigation, data curation. B.M. investigation and data curation, E.R.C. Investigation, data curation, writing&review and editing, A.M., F.C. writing&review and editing, project administration, and funding acquisition.



## Conflicts of interest

View Article Online  
DOI: 10.1039/D6TA01464J

The authors declare no competing financial interest.

## Data availability

The authors confirm that the data supporting the findings of this study are available within the article and its supplementary information (SI). Supplementary information is available.

## Acknowledgments

This work has been funded by the European Union - NextGenerationEU under the Italian Ministry of University and Research (MUR) National Innovation Ecosystem grant ECS00000041 - VITALITY. We acknowledge Università degli Studi di Perugia and MUR for support within the project Vitality and the Fondazione Perugia through Bando di Ricerca Scientifica 2023 (ID21101). A.D and A.M. thank also the funding from Fondo Ricerca di Ateneo, edition 2021. G.M.R. and A.M. thank also the funding from the Presidency of the Council of Ministers of Italy - Department for Cohesion Policies and the South, under the UMBriaTECH – Umbria Materials TECHnology project (CUP E67G23000220001). B.M. thank also the Center for Electronic Microscopy (Ce.ME) - Laura Bonzi at the ICCOM-CNR in Florence. E.R.C. thanks the financial support of project PID2021-126235OB-C32 funded by MCIN/ AEI/10.13039/501100011033/ and FEDER funds, and the financial support of UNICAJA and Erasmus+ for H2EXCELLENCE.



## References

View Article Online  
DOI: 10.1039/D6TA01464J

- 1 I. Dincer, *Int. J. Hydrogen Energy*, 2012, **37**, 1954–1971.
- 2 M. Awad, A. Said, M. H. Saad, A. Farouk, M. M. Mahmoud, M. S. Alshammari, M. L. Alghaythi, S. H. E. Abdel Aleem, A. Y. Abdelaziz and A. I. Omar, *Alexandria Eng. J.*, 2024, **87**, 213–239.
- 3 J. Song, C. Wei, Z.-F. Huang, C. Liu, L. Zeng, X. Wang and Z. J. Xu, *Chem. Soc. Rev.*, 2020, **49**, 2196–2214.
- 4 G. Menendez Rodriguez and A. Macchioni, *Eur. J. Inorg. Chem.*, 2023, **26**, e202200625.
- 5 L. Gao, X. Cui, C. D. Sewell, J. Li and Z. Lin, *Chem. Soc. Rev.*, 2021, **50**, 8428–8469.
- 6 L. Fagiolari, F. Zaccaria, F. Costantino, R. Vivani, C. K. Mavrokefalos, G. R. Patzke and A. Macchioni, *Dalton Trans.*, 2020, **49**, 2468–2476.
- 7 L. Baldinelli, G. Menendez Rodriguez, I. D'Ambrosio, A. M. Grigoras, R. Vivani, L. Latterini, A. Macchioni, F. De Angelis and G. Bistoni, *Chem. Sci.*, 2024, **15**, 1348–1363.
- 8 P. Roy Chowdhury, H. Medhi, K. G. Bhattacharyya and C. M. Hussain, *Coord. Chem. Rev.*, 2024, **501**, 215547.
- 9 L. Fagiolari and A. Macchioni, in *Progress in Layered Double Hydroxides from Synthesis to New Applications*, ed. K. M. Kadish and R. Guilard, Series on Chemistry, Energy and the Environment, vol. 8, World Scientific Publishing, Singapore, 2022, ch. 5.
- 10 M. Zubair, M. M. Ul Hassan, M. T. Mehran, M. M. Baig, S. Hussain and F. Shahzad, *Int. J. Hydrogen Energy*, 2022, **47**, 2794–2818.
- 11 B. He, F. Bai, P. Jain and T. Li, *Small*, 2025, **21**, 2411479.
- 12 Y. Luo, X. Li, X. Cai, X. Zou, F. Kang, H.-M. Cheng and B. Liu, *ACS Nano*, 2018, **12**, 4565–4573.
- 13 K. B. Ibrahim, T. A. Shifa, M. Bordin, E. Moretti, H.-L. Wu and A. Vomiero, *Small Methods*, 2023, **7**, 202300348.



- 14 Y. Pu, M. J. Lawrence, V. Celorrio, Q. Wang, M. Gu, Z. Sun, L. A. Jácome, A. E. Russell, L. Huang and P. Rodriguez, *J. Mater. Chem. A*, 2020, **8**, 13340–13349. View Article Online  
DOI: 10.1039/D0TA01464J
- 15 C. Tang, H.-S. Wang, H.-F. Wang, Q. Zhang, G.-L. Tian, J.-Q. Nie and F. Wei, *Adv. Mater.*, 2015, **27**, 4516–4522.
- 16 J. Sanchez, M. Burke Stevens, A. R. Young, A. Gallo, M. Zhao, Y. Liu, M. V. Ramos-Garcés, M. Ben-Naim, J. L. Colón, R. Sinclair, L. A. King, M. Bajdich and T. F. Jaramillo, *Adv. Energy Mater.*, 2021, **11**, 2003545.
- 17 M. V. Ramos-Garcés and J. L. Colón, *Nanomaterials*, 2020, **10**, 822.
- 18 M. V. Ramos-Garcés, J. Sanchez, D. E. Del Toro-Pedrosa, I. B. Alvarez, Y. Wu, E. Valle, D. Villagrán, T. F. Jaramillo and J. L. Colón, *ACS Appl. Energy Mater.*, 2019, **2**, 3561–3567.
- 19 M. V. Ramos-Garcés, J. Sanchez, K. La Luz-Rivera, D. E. Del Toro-Pedrosa, T. F. Jaramillo and J. L. Colón, *Dalton Trans.*, 2020, **49**, 3892–3900.
- 20 R. Vivani, F. Costantino and M. Taddei, in *Metal Phosphonate Chemistry*, ed. A. Clearfield and K. D. Demadis, Royal Society of Chemistry, London, 2011, pp. 45–86.
- 21 A. Donnadio, M. Nocchetti, F. Costantino, M. Taddei, M. Casciola, F. da Silva Lisboa and R. Vivani, *Inorg. Chem.*, 2014, **53**, 13220–13226.
- 22 M. Nocchetti, A. Donnadio, E. Vischini, T. Posati, C. Albonetti, D. Campoccia, C. R. Arciola, S. Ravaioli, V. Mariani, L. Montanaro and R. Vivani, *Inorg. Chem.*, 2022, **61**, 2251–2264.
- 23 F. Costantino, R. Vivani, M. Bastianini, L. Ortolani, O. Piermatti, M. Nocchetti and L. Vaccaro, *Chem. Commun.*, 2015, **51**, 15990–15993.
- 24 V. Kozell, T. Giannoni, M. Nocchetti, R. Vivani, O. Piermatti and L. Vaccaro, *Catalysts*, 2017, **7**, 186.
- 25 F. Costantino, M. Nocchetti, M. Bastianini, A. Lavacchi, M. Caporali and F. Liguori, *ACS Appl. Nano Mater.*, 2018, **1**, 1750–1757.



- 26 M. Nocchetti, A. Donnadio, E. Vischini, T. Posati, S. Ravaoli, C. R. Arciola, D. Campoccia and R. Vivani, *Materials*, 2019, **12**, 3185. View Article Online  
DOI: 10.1039/D6TA01464J
- 27 K. Moedritzer and R. R. Irani, *J. Org. Chem.*, 1966, **31**, 1603–1607.
- 28 C. C. L. McCrory, S. Jung, J. C. Peters and T. F. Jaramillo, *J. Am. Chem. Soc.*, 2013, **135**, 16977–16987.
- 29 Y. Q. Gao, X. Y. Liu and G. W. Yang, *Nanoscale*, 2016, **8**, 5015–5023.
- 30 G. Alberti, R. Bertrami and U. Costantino, *J. Inorg. Nucl. Chem.*, 1976, **38**, 1729–1732.
- 31 J.F. Moulder, W.F. Stickle, P.E. Sobol and K.D. Bomben . Handbook of X-ray Photoelectron Spectroscopy. (J. Chastain & R. C. King Jr., Eds.), 1995. Physical Electronics Division, Perkin-Elmer Corp.
- 32 M. Descostes, F. Mercier, N. Thromat, C. Beaucaire and M. Gautier-Soyer, *Appl. Surf. Sci.*, 2000, **165**, 288-302.
- 33 E. Fabbri, A. Habereeder, K. Waltar, R. Kötz and T. J. Schmidt, *Catal. Sci. Technol.*, 2014, **4**, 3800–3821.
- 34 M. S. Burke, M. G. Kast, L. Trotochaud, A. M. Smith and S. W. Boettcher, *J. Am. Chem. Soc.*, 2015, **137**, 3638–3648.
- 35 M. W. Louie and A. T. Bell, *J. Am. Chem. Soc.*, 2013, **135**, 12329–12337.
- 36 S. Anantharaj, P.E Karthik and S. Noda, *Angew. Chem. Int. Ed.* 2021, **60**, 23051–23067.
- 37 M. Schulze, R. Reissner, M. Lorenz, U. Radke and W. Schnurnberge, *Electrochim. Acta*, 1999, **44**, 3969-3976.

